PHYSICAL REVIEW B **102**, 195134 (2020)

Pyrochlore iridates: Electronic and magnetic structures, x-ray magnetic circular dichroism, and resonant inelastic x-ray scattering

V. N. Antonov,[1] L. V. Bekenov,[1] and D. A. Kukusta[1,2]
[1]G. V. Kurdyumov Institute for Metal Physics of the N.A.S. of Ukraine, 36 Academician Vernadsky Boulevard, UA-03142 Kyiv, Ukraine
[2]Max-Planck-Institut für Festkörperforschung, Heisenberg Strasse 1, D-70569 Stuttgart, Germany

(Received 18 September 2020; accepted 4 November 2020; published 19 November 2020)

We have investigated the electronic and magnetic properties of the pyrochlore iridates $Y_2Ir_2O_7$, $Pr_2Ir_2O_7$, and $Eu_2Ir_2O_7$ within the density-functional theory (DFT) using the generalized gradient approximation with taking into account strong Coulomb correlations (GGA+U) in the framework of the fully relativistic spin-polarized Dirac linear muffin-tin orbital band-structure method. The x-ray absorption spectra (XAS) and x-ray magnetic circular dichroism (XMCD) at the Ir $L_{2,3}$, Pr $L_{2,3}$, Pr $M_{4,5}$, and O K edges in the pyrochlore iridate $Pr_2Ir_2O_7$ have been investigated theoretically from first principles. The calculated results are in good agreement with experimental data. We have also investigated theoretically the resonant inelastic x-ray scattering (RIXS) spectra at the Ir L_3 edge in the pyrochlore iridates $R_2Ir_2O_7$ (R = Y, Pr, and Eu). We have found that these materials exhibit qualitatively similar excitation spectra. The experimentally measured RIXS spectra of all three compounds in addition to the elastic scattering peak at 0 eV possess sharp features below 2 eV corresponding to transitions within the Ir t_{2g} levels, and a strong intense peak stretching from 2.5 to 5 eV that according to the calculations corresponds to d-d transitions between the Ir t_{2g} and e_g manifolds. We have found that the double peak at low energy can be assigned to local excitations between the filled $J_{\rm eff} = 1/2$ and empty $J_{\rm eff} = 1/2$ manifolds; the latter states are split into two subbands.

DOI: 10.1103/PhysRevB.102.195134

I. INTRODUCTION

The pyrochlore iridates $R_2Ir_2O_7$ (R=Y or rare-earth lanthanides) provide many interesting properties and have received considerable attention in recent years due to a unique combination of extended 5d orbitals, strong electronic correlations, large spin-orbit (SO) coupling, and geometric frustration [1–4]. The frustration mainly arises due to interpenetrating tetrahedra, where the magnetic ions sitting at the vertices of the tetrahedra introduce magnetic frustration for antiferromagnetic (AFM) interactions. Many interesting phases and phenomena have been proposed in the pyrochlore iridates [5] recently, such as a topological band insulator [6,7], a topological Mott insulator [6,8], an axion insulator [9,10], new topological phases, such as the Weyl semimetal state [11–15], a novel metallic spin liquid ground state, an anomalous Hall effect [16–18], and others. Despite the fruitful achievements, the unique physical properties of these systems have not been fully understood yet.

We focus on $R_2Ir_2O_7$ pyrochlore iridates with R = Pr and Eu, as well as $Y_2Ir_2O_7$ as a reference compound. The latter pyrochlore iridate has nonmagnetic Y^{3+} ($4d^0$) at the A site and shows an insulating behavior and an AFM-type magnetic transition with ordering temperature $T_N \sim 160$ K [19–24]. Given magnetically inactive Y^{3+}, this magnetic ordering is only associated with the Ir sublattice. The magnetic state in $Y_2Ir_2O_7$ has been investigated using muon spin relaxation (μSR) measurements, which indicate a magnetic long-range ordering at low temperature [19]. However, the neutron powder diffraction (NPD) measurements show no sign of such an ordering within the sensitivity of the instrumentation. These measurements do not rule out long-range magnetic order, because iridium is a strong absorber of neutrons, therefore the NPD measurements remain largely insensitive for Ir-containing materials [20]. The $Pr_2Ir_2O_7$ is another interesting compound in pyrochlore iridates which has a magnetic and comparatively large A-site ion, Pr^{3+} ($4f^2$). This material has two active (Pr and Ir) sublattices, behaves as a spin liquid, and has no long-range magnetic order down to 0.3 K [3,25]. In addition, the $Pr_2Ir_2O_7$ thin film shows a spontaneous Hall effect without an applied magnetic field and without possessing spontaneous magnetization [26,27]. The spontaneous Hall effect is not caused by the conventional mechanism of the anomalous Hall effect that is related to ferromagnetism but has an unconventional origin related to the noncoplanar or noncollinear spin texture. $Pr_2Ir_2O_7$ has a Fermi node formed by a quadratic band touching of the doubly-degenerate valence and conduction bands at the Γ point at the Fermi level, called as a Luttinger semimetal state [18,28]. This nodal state is sensitive to perturbation by strain and can be manipulated to give rise to other topological phases such as a topological insulator or a Weyl semimetal by breaking the cubic and/or the time reversal symmetry [18,27,28]. The value of resistivity for $Pr_2Ir_2O_7$ was found to be very low, and it decreases continuously with decreasing temperature down to 50 K showing a metallic behavior [29]. At low temperature below 50 K, a small rise in the resistivity of $Pr_2Ir_2O_7$ was observed down to 12 K. We can conclude that $Pr_2Ir_2O_7$ is on the border between a narrow semiconductor and a semimetal. Similar results were obtained by Ohtsuki *et al.* [27] on high quality (111)-oriented pyrochlore $Pr_2Ir_2O_7$ epitaxial thin films: As the temperature is lowered from room temperature, the resistivity ρ_{xx} monotonically decreases at first, indicating metallic conductivity. It then shows an upturn after reaching a minimum around 50 K showing the semiconducting behavior below this temperature. Similar features in the temperature dependence of ρ_{xx}, i.e., a minimum and an upturn toward 0 K, have been observed in other metallic pyrochlore iridates [3,30,31]. However, the origin of them is still controversial [27].

Krajewska *et al.* [32] synthesized recently a new pyrochlore iridate $In_2Ir_2O_7$ with a nonmagnetic In^{3+} ion occupying the A site. The In^{3+} ion has the smallest A-site ionic radius (0.92 Å) among reported $A_2Ir_2O_7$ pyrochlores and renders the most distorted IrO_6 octahedra with the largest trigonal compression and the smallest Ir-O-Ir angle of 125.8° among pyrochlore iridates. The authors found that the pyrochlore iridate $In_2Ir_2O_7$ is a $J_{\text{eff}} = 1/2$ Mott insulator with frustrated magnetism. Despite the large trigonal distortion, only a small admixture of the $J_{\text{eff}} = 3/2$ component in the $J_{\text{eff}} = 1/2$ bands was observed as compared with other pyrochlore iridates $A_2Ir_2O_7$. The authors argue that a predominant role in the distinct behavior of $In_2Ir_2O_7$ plays reduced intersite hopping between the $J_{\text{eff}} = 1/2$ and $J_{\text{eff}} = 3/2$ manifolds due to the large trigonal distortion and the covalent character of In-O bonds.

Shinaoka *et al.* [33] study the prototype 5*d* pyrochlore iridate $Y_2Ir_2O_7$ from first principles using the combining density functional theory (DFT) and embedded dynamical mean-field theory (DMFT) methods (DFT + DMFT). They map out the phase diagram in the space of temperature, onsite Coulomb repulsion U, and filling. They found that an all-in-all-out (AIAO) ordered insulating phase is stable for realistic values of U. Zhang *et al.* [34] apply the DFT + DMFT method to study the metal-insulator transition in $R_2Ir_2O_7$ (R = Y, Eu, Sm, Nd, Pr, and Bi). They found that the metal-insulator transition occurs for an A-cation radius between that of Nd and Pr, in agreement with experiments. The AIAO magnetic phase, which is stable in the Nd compound but not the Pr one, opens a sizable correlated gap.

Since the R and Ir cations are both magnetically active, the use of element-resolved x-ray absorption, x-ray magnetic circular dichroism (XMCD), and resonant inelastic x-ray scattering (RIXS) spectroscopies is natural to explore individual R and Ir sublattices. The RIXS spectra in the pyrochlore iridates at the Ir L_3 edge were measured by several authors. Hozoi *et al.* [35] provide the measurements of the RIXS spectra in $Y_2Ir_2O_7$ and $Eu_2Ir_2O_7$. Uematsu *et al.* [36] also reported Ir $L_{2,3}$ RIXS spectra in $Eu_2Ir_2O_7$. They found a large suppression of the magnetic scattering signal at the Ir L_2 edge which supports the $J_{\text{eff}} = 1/2$ picture in this compound. Donnerer *et al.* [37] investigated the RIXS spectra in close vicinity of the Ir L_3 edge to address the unresolved nature of the magnetic ground state in $Sm_2Ir_2O_7$. Krajewska *et al.* [32] present the Ir L_3 edge RIXS spectrum of recently synthesized new pyrochlore iridate $In_2Ir_2O_7$. Clancy *et al.* [38] investigated the structural, electronic, and magnetic properties of the pyrochlore iridates $Eu_2Ir_2O_7$ and $Pr_2Ir_2O_7$ using a combination of resonant elastic x-ray scattering, x-ray powder diffraction, and RIXS as a function of temperature and applied pressure. They found no evidence of crystal symmetry change over a wide range of temperatures and pressures studied. In spite of very different ground state properties, these two materials exhibit qualitatively similar RIXS spectra at the Ir L_3 edge. Kumar *et al.* [24] investigated the evolution of structural, magnetic, and transport properties in solid solution pyrochlore iridates $(Y_{1-x}Pr_x)_2Ir_2O_7$ ($x = 0 - 1$). With Y substitution, the magnetic-insulating state in $Y_2Ir_2O_7$ ($x = 0.0$) is weakened, while $Pr_2Ir_2O_7$ ($x = 1.0$) shows a paramagnetic-metallic behavior. A metal-insulator transition is observed for the $x = 0.8$ sample. The authors also presented the x-ray absorption spectra (XAS) at the Ir L_3, Pr $M_{4,5}$, and O K edges. Guo *et al.* [39] measured the XAS and XMCD spectra at the Ir $L_{2,3}$ and Pr L_3 edges in films and powder samples of $Pr_2Ir_2O_7$.

In the present study, we investigate theoretically the electronic and magnetic properties, the XAS, XMCD, and RIXS spectra in the pyrochlore iridates $R_2Ir_2O_7$ (R = Y, Pr, and Eu) from first principles. The energy band structure of $R_2Ir_2O_7$ in this paper is calculated within the *ab initio* approach by applying the generalized gradient approximation (GGA) using the fully relativistic spin-polarized Dirac linear muffin-tin orbital band-structure method with taking into account strong electron-electron correlations.

The paper is organized as follows. The crystal structure of the pyrochlore iridates and computational details are presented in Sec. II. Section III presents the electronic and magnetic structures of the $R_2Ir_2O_7$ (R=Y, Pr, and Eu) compounds. Section IV presents the theoretical investigations of the RIXS spectra of the $R_2Ir_2O_7$ (R=Y, Pr, and Eu) compounds as well as the solid solution pyrochlore iridates $(Y_{1-x}Pr_x)_2Ir_2O_7$ ($x = 0.75$ and 0.5) at the Ir L_3 edge. Section V is devoted to the XAS and XMCD spectra of the $Pr_2Ir_2O_7$ compound at the Ir $L_{2,3}$, Pr $L_{2,3}$ and $M_{4,5}$, and O K edges; the theoretical results are compared with experimental measurements. Finally, the results are summarized in Sec. VI.

II. COMPUTATIONAL DETAILS

A. Crystal structure

The pyrochlore $R_2Ir_2O_7$ crystallizes in the cubic space group $Fd\bar{3}m$ (Fig. 1), with A-site atoms at the 16*d* position (0.5, 0.5, 0.5), Ir at the 16*c* position (0, 0, 0), O_1 at the 48*f* (x, 0.125, 0.125), and O_2 at the 8*a* (0.375, 0.375, 0.375). In each unit cell there are eight formula units. Only two parameters in this structure, namely the lattice constant a and the x coordinate associated with the O_1 site, are adjustable. The positional parameter x provides a measure of the distortion of the IrO_6 octahedra, with $x_c = 5/16 = 0.3125$ corresponding to ideal undistorted octahedra. For $x > 5/16$ the IrO_6 octahedra become trigonally compressed, while for $x < 5/16$ they become trigonally elongated. All pyrochlore iridates have x larger than the value for ideal IrO_6 octahedra x_c, indicating that a compressive trigonal distortion is present with the Ir-O-Ir angle reduced from ideal ~141°. Larger A-site ions tend to result in a smaller distortion, which is believed to be responsible for increased hopping and a stronger metallic character [14,32,38]. The unit-cell parameters a in pyrochlore iridium compounds $R_2Ir_2O_7$ are

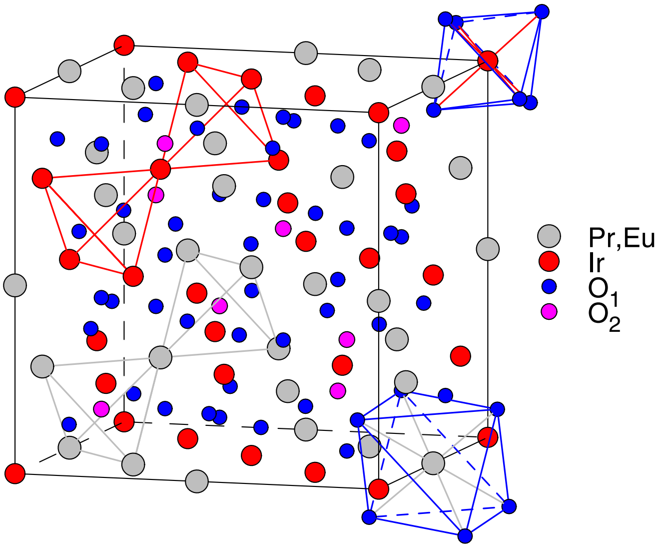

FIG. 1. The crystal structure of the pyrochlore iridates $Eu_2Ir_2O_7$ and $Pr_2Ir_2O_7$ (the space group is $Fd\bar{3}m$, No. 227). Red spheres represent iridium atoms, blue and magenta spheres show oxygen atoms, gray spheres represent Pr/Eu atoms. The Pr/Eu and Ir sublattices form a network of corner-sharing tetrahedra. Each Ir atom lies at the center of a trigonally compressed IrO_6 octahedron, surrounded by a hexagonal ring of Eu/Pr atoms.

equal to 10.244 Å, 10.4145 Å, and 10.274 Å for R = Y, Pr and Eu, respectively [16,24].

Clancy *et al.* [38] present the pressure dependence of the cubic lattice constant a and the x coordinate of the O_1 atom for $Eu_2Ir_2O_7$ up to 17 GPa. A small, but finite, increase in x is clearly observed, suggesting that the IrO_6 octahedra become increasingly more distorted at higher pressures. The authors observe no pressure-induced structural transitions or symmetry changes for applied pressures up to 17 GPa. This result has direct implications for recent high-pressure transport studies by Tafti *et al.* [30], who reported a pressure-induced metal-insulator (low temperature) transition in $Eu_2Ir_2O_7$ around 6–8 GPa. Since the experimental results of Clancy *et al.* [38] demonstrated that no structural anomalies occur in the vicinity of the critical pressure, we can conclude that these pressure-induced transitions are likely driven by purely electronic effects.

The key to the intriguing properties of $R_2Ir_2O_7$ is the intimate coupling of two interpenetrating cation sublattices, the rare earth with highly frustrated magnetic moments, and the iridium with extended conduction orbitals significantly mixed by the spin-orbit interaction, as well as connecting oxygens. Each sublattice consists of alternating triangular and Kagome planes that are more easily visualized as forming a cornersharing tetrahedra network (Fig. 1). The high coordination of the lattice allows significant overlap of Ir orbitals simultaneous with frustrated magnetism of the R ions.

B. Resonant inelastic x-ray scattering

Resonant inelastic x-ray scattering refers to the process where the material first absorbs a photon. The system then is excited to a short-lived intermediate state, from which it relaxes radiatively. In an experiment, one studies the x rays emitted in this decay process. The RIXS intensity can in general be presented in terms of a scattering amplitude as [40]

$$I(\omega,\mathbf{k},\mathbf{k}',\boldsymbol{\epsilon},\boldsymbol{\epsilon}') = \sum_f |T_{fg}(\mathbf{k},\mathbf{k}',\boldsymbol{\epsilon},\boldsymbol{\epsilon}',\omega_{\mathbf{k}})|^2 \times \delta(E_f + \hbar\omega_{\mathbf{k}'} - E_g - \hbar\omega_{\mathbf{k}}), \tag{1}$$

where the delta function enforces energy conservation and the amplitude $T_{fg}(\mathbf{k},\mathbf{k}',\boldsymbol{\epsilon},\boldsymbol{\epsilon}',\omega_{\mathbf{k}})$ reflects which excitations are probed and how, for instance, the spectral weights of final state excitations depend on the polarization vectors $\boldsymbol{\epsilon}$ and $\boldsymbol{\epsilon}'$ of the incoming and outgoing x rays, respectively.

In the direct RIXS process [40] the incoming photon with energy $\hbar\omega_{\mathbf{k}}$, momentum $\hbar\mathbf{k}$, and polarization $\boldsymbol{\epsilon}$ excites the solid from the ground state $|\mathrm{g}\rangle$ with energy E_{g} to the intermediate state $|\mathrm{I}\rangle$ with energy E_{I}. During relaxation the outcoming photon with energy $\hbar\omega_{\mathbf{k}'}$, momentum $\hbar\mathbf{k}'$, and polarization $\boldsymbol{\epsilon}'$ is emitted, and the solid is in the state $|\mathrm{f}\rangle$ with energy E_{f}. As a result an excitation with energy $\hbar\omega = \hbar\omega_{\mathbf{k}} - \hbar\omega_{\mathbf{k}'}$ and momentum $\hbar\mathbf{q} = \hbar\mathbf{k} - \hbar\mathbf{k}'$ is created. Our implementation of the code for calculation of the RIXS intensity uses Dirac four-component basis functions [41] in the perturbative approach [42,43]. RIXS is the second-order process, and its intensity is given by

$$I(\omega,\mathbf{k},\mathbf{k}',\boldsymbol{\epsilon},\boldsymbol{\epsilon}') \propto \sum_{\mathrm{f}} \left| \sum_{\mathrm{I}} \frac{\langle \mathrm{f}|\hat{H}'_{\mathbf{k}'\boldsymbol{\epsilon}'}|\mathrm{I}\rangle\langle \mathrm{I}|\hat{H}'_{\mathbf{k}\boldsymbol{\epsilon}}|\mathrm{g}\rangle}{E_{\mathrm{g}} - E_{\mathrm{I}}} \right|^2 \times \delta(E_{\mathrm{f}} - E_{\mathrm{g}} - \hbar\omega), \tag{2}$$

where the RIXS perturbation operator in the dipole approximation is given by the lattice sum $\hat{H}'_{\mathbf{k}\boldsymbol{\epsilon}} = \sum_{\mathbf{R}} \hat{\boldsymbol{\alpha}}\boldsymbol{\epsilon}\exp(-i\mathbf{k}\mathbf{R})$, where α are the Dirac matrices. The sum over the intermediate states $|\mathrm{I}\rangle$ includes the contributions from different spin-split core states at the given absorption edge. Both $|\mathrm{g}\rangle$ and $|\mathrm{f}\rangle$ states are dispersive so the sum over final states is calculated using the linear tetrahedron method [44,45]. The detailed expressions of the matrix elements in the electric dipole approximation in the framework of the fully relativistic Dirac representation were presented in Ref. [46].

C. Calculation details

The details of the computational method are described in our previous papers [47–50] and here we only mention several aspects. The band structure calculations were performed using the fully relativistic linear muffin-tin orbital (LMTO) method [51,52]. This implementation of the LMTO method uses four-component basis functions constructed by solving the Dirac equation inside an atomic sphere [41]. The exchange-correlation functional of a GGA-type was used in the version of Perdew, Burke, and Ernzerhof (PBE) [53]. The Brillouin zone (BZ) integration was performed using the improved tetrahedron method [45]. The basis consisted of R and Ir s, p, d, and f, and O s, p, and d LMTO's.

To take into account electron-electron correlation effects we used in this work the "relativistic" generalization of the rotationally invariant version of the LSDA+U method [54] which takes into account SO coupling so that the occupation matrix of localized electrons becomes nondiagonal in spin indexes. The screened Coulomb U and exchange Hund coupling J_H integrals enter the LSDA+U energy functional as external parameters and have to be determined independently. These parameters can be determined from supercell LSDA calculations using Slater's transition state technique [55,56], from constrained LSDA calculations (cLSDA) [56–60], or from the constrained random-phase approximation (cRPA) scheme [61]. Subsequently, a combined cLSDA and cRPA method was also proposed [62]. The cLSDA calculations produce $J_H = 0.7$ eV for $4f$ states at the Pr and Eu sites in $Pr_2Ir_2O_7$ and $Eu_2Ir_2O_7$. It is known that the cRPA method underestimates values of U in some cases [63]. On the other hand, the cLSDA method produces too large values of U [64]. Therefore, in our calculations we treated the Hubbard U as an external parameter and varied it from 3.0 to 8.0 eV. We found relatively small sensitivity of the RIXS, XAS, and XMCD spectra to the value of U. We use $U = 7$ eV and $J_H = 0.7$ eV ($U_{\text{eff}} = 6.3$ eV) for $4f$ states at the Pr and Eu sites in our calculations which are typical for $4f$ correlated systems [65]. We use the value of $U_{\text{eff}} = 1.5$ eV for $3d$ states at the Ir site ($U = 2.1$ eV and $J_H = 0.6$ eV) which gives the best agreement between the calculated and experimental XAS, XMCD, and optical spectra in β-Li_2IrO_3 [66].

The XAS and XMCD spectra were calculated with taking into account the core-hole effect within the supercell approximation [67] and the exchange splitting of core levels. The finite lifetime of a core hole was accounted for by folding the spectra with a Lorentzian. The widths of core levels were taken from Ref. [68]. The finite experimental resolution of the spectrometer was accounted for by a Gaussian of 0.6 eV width. Although, it is widely believed that the d-d excitations show only a small momentum transfer vector $\mathbf{Q}$ dependence in transition metal oxides [32], we choose in our RIXS calculations the vector $\mathbf{Q}$ used in the corresponding RIXS measurements, namely, $\mathbf{Q} = (8.45, 8.45, 7.0)$ for $Y_2Ir_2O_7$ [35] and $\mathbf{Q} = (7.5, 7.5, 7.5)$ for $Pr_2Ir_2O_7$ and $Eu_2Ir_2O_7$ [38].

III. ELECTRONIC AND MAGNETIC STRUCTURES

A. Electronic structure

Figure 2 presents the *ab initio* energy band structure of $Y_2Ir_2O_7$ in the energy range from −1.4 to 0.8 eV, calculated in the fully relativistic Dirac GGA+SO approximation (the upper panel) and with taking into account Coulomb correlations in the GGA+SO+U approximation (the lower panel). The GGA+SO bands are presented by circles proportional in size to their orbital character projected onto the basis set of Ir $d_{3/2}$ (blue) and $d_{5/2}$ (red) states.

Each Ir^{4+} ion in $Y_2Ir_2O_7$ surrounded by six O^{2-} ions has five valent $5d$ electrons. The octahedral crystal field largely splits the Ir t_{2g} and e_g manifolds, so that all five electrons occupy the t_{2g} manifold. The strong SO coupling splits the t_{2g} manifold into a completely filled lower $J_{\text{eff}} = 3/2$ quartet and a half-occupied upper $J_{\text{eff}} = 1/2$ doublet. The functions of the $J_{\text{eff}} = 3/2$ quartet are dominated by $d_{3/2}$ states with some minor weight of $d_{5/2}$ ones, which is determined by the relative strengths of SO coupling and crystal-field splitting. The $J_{\text{eff}} = 1/2$ functions, on the other hand, are given by linear combinations of $d_{5/2}$ states only. This allows one to identify the bands with pure $d_{5/2}$ character as originating from $J_{\text{eff}} = 1/2$ states.

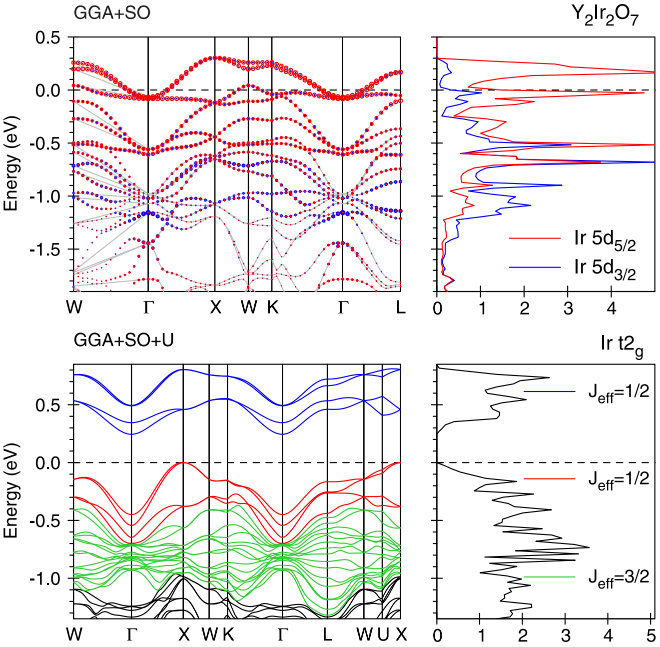

FIG. 2. The *ab initio* energy band structure and Ir $5d$ partial DOS [in states/(atom eV)] of $Y_2Ir_2O_7$ calculated in the fully relativistic Dirac GGA+SO approximation (upper panel, colors represent dominant orbital character as marked in the legend) and with taking into account Coulomb correlations in the GGA+SO+U approximation (lower panel).

The GGA+SO approximation produces a metallic ground state in $Y_2Ir_2O_7$, in contradiction with resistivity measurements which claim that $Y_2Ir_2O_7$ is a Mott insulator. To produce the insulating ground state we use the GGA+U method. The Coulomb repulsion U splits the half-filled $J_{\text{eff}} = 1/2$ band into an empty upper energy band (blue lines in the lower panel of Fig. 2) and a lower energy band (red lines in the lower panel of Fig. 2). The pyrochlore iridate $Y_2Ir_2O_7$ is a $J_{\text{eff}} = 1/2$ insulator with frustrated magnetism. We found only a small admixture of the $J_{\text{eff}} = 3/2$ component in the $J_{\text{eff}} = 1/2$ bands in this compound.

With increasing the size of A cations from Y^{3+} to Pr^{3+}, the system becomes a semimetal and remains metallic down to the lowest temperature [3,28]. Figure 3 presents the energy band structure of $Pr_2Ir_2O_7$ calculated in the GGA+SO and GGA+SO+U approximations (the upper and middle panels, respectively). Comparing the upper panels of Figs. 2 and 3 we can conclude that the admixture of the $J_{\text{eff}} = 3/2$ component to the $J_{\text{eff}} = 1/2$ states is increased with going from $Y_2Ir_2O_7$ to $Pr_2Ir_2O_7$.

Our GGA+SO+U calculations produce the semimetallic solution in $Pr_2Ir_2O_7$ (the middle panel of Fig. 3) in agreement with the experimental data [3,27–29]. We also investigated the evolution of the electronic structure in the solid solution pyrochlore iridates $(Y_{1-x}Pr_x)_2Ir_2O_7$ ($x = 0$, 0.75, and 0.5). With Y substitution the magnetic-insulating state in

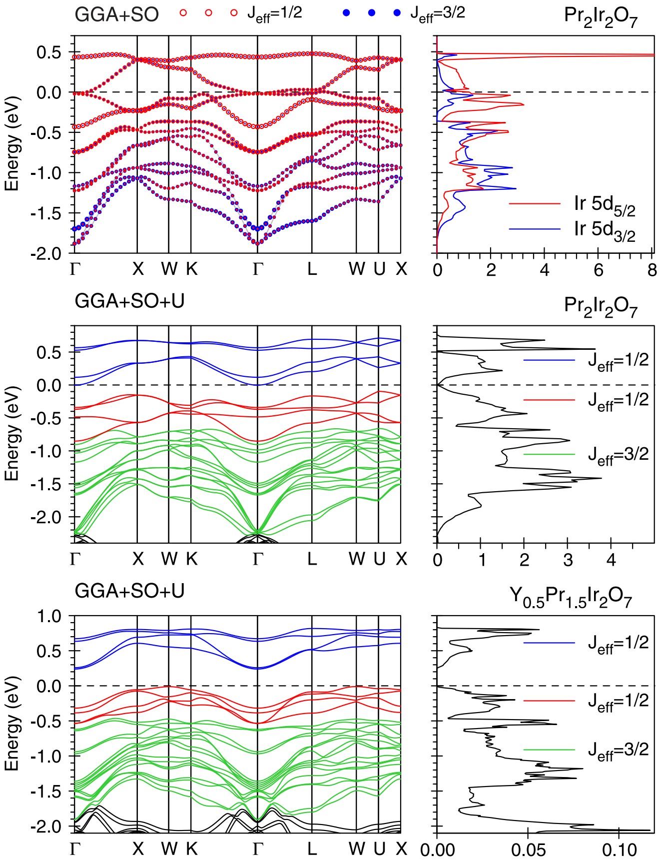

FIG. 3. The *ab initio* energy band structure and Ir 5d partial DOS [in states/(atom eV)] of $Pr_2Ir_2O_7$ calculated in the fully relativistic Dirac GGA+SO approximation (upper panel) and with taking into account Coulomb correlations in the GGA+SO+U approximation (middle panel). The lower panel presents the energy band structure of $Y_{0.5}Pr_{1.5}Ir_2O_7$ in the GGA+SO+U approximation.

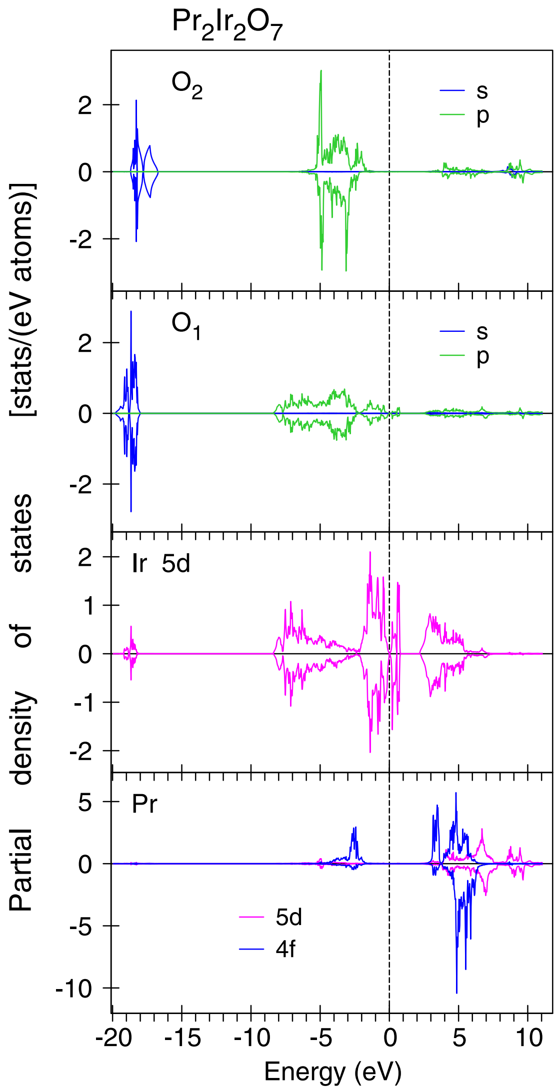

FIG. 4. The partial DOSs of $Pr_2Ir_2O_7$ calculated in the GGA+SO+U approximation.

$Y_2Ir_2O_7$ ($x = 0.0$) is weakened, and $(Y_{1-x}Pr_x)_2Ir_2O_7$ possesses a metal-insulator transition for $x = 0.75$ (see the lower panel in Fig. 3). It is in agreement with the Kumar *et al.* [24] measurements who observed a metal-insulator transition for the $x = 0.8$ sample.

Figures 4 and 5 present the total and partial density of states of $Pr_2Ir_2O_7$ and $Eu_2Ir_2O_7$, respectively, in the GGA+SO+U approximation. The O 2s states are located mostly between −18.5 and −16.5 eV below the Fermi level in both compounds. The occupied part of the 2p states of O is found from −6 to −1.5 eV in $Pr_2Ir_2O_7$ and from −7 to −2 eV in $Eu_2Ir_2O_7$. The spin splitting of the O p states is quite small. The Ir 5d states are very similar in both compounds with t_{2g} states situated from −2 eV to 0.8 eV and e_g states in the 2.5 eV to 5.5 eV energy interval. The occupied Pr 4f states are situated from −3 eV to −2.3 eV in $Pr_2Ir_2O_7$ with empty 4f states between 3 eV and 6.4 eV slightly overlapped with empty Ir 5d states. The $Eu_2Ir_2O_7$ compound possesses the Eu 4f spin-up states at −7.3 eV to −4.7 eV and spin-down ones at 3.8 eV to 6.3 eV. Besides, there is a narrow 4f spin-up peak situated between the Ir t_{2g} and e_g states from 1.1 to 1.4 eV above the Fermi level.

The hybridization between the Ir 5d and rare earth 4f states is rather weak, therefore, the quasicore approximation is valid in these compounds. The GGA+SO+U approach and the fully localized 4f-in-core model produce almost identical energy bands in close vicinity of the Fermi level (compare the energy bands in the upper and lower panels of Fig. 6). Only the top of the Ir e_g states are slightly modified due to overlaps with the Eu 4f states above 4 eV. It is interesting to note also that the structure of the Ir t_{2g} energy bands is almost identical in $Eu_2Ir_2O_7$ and $Pr_2Ir_2O_7$ (compare the lower panel of Fig. 6 and the middle panel of Fig. 3). This fact explains why these two compounds exhibit qualitatively similar RIXS spectra (see Fig. 9 below). Another very important feature is the split of the empty upper energy bands ($J_{\text{eff}} = 1/2$) in all three compounds under consideration (blue bands in the lower panel of Fig. 2, the middle panel of Fig. 3, and the upper panel of Fig. 6). The split is the smallest in $Y_2Ir_2O_7$ and the largest in $Eu_2Ir_2O_7$. Such a splitting is responsible for the double peak structure at low energy in the corresponding RIXS spectra (see Fig. 9 below).

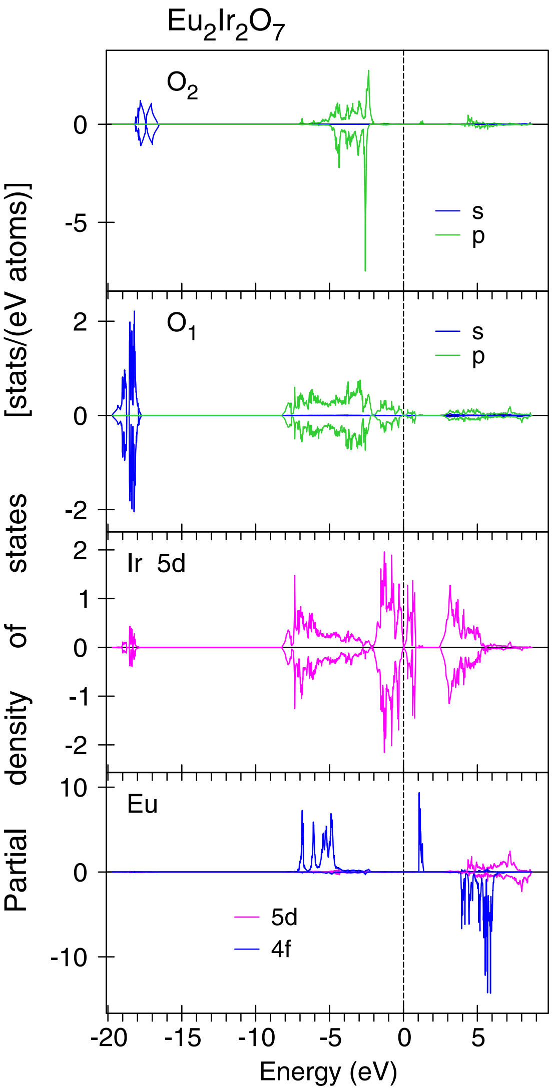

FIG. 5. The partial DOSs of $Eu_2Ir_2O_7$ calculated in the GGA+SO+U approximation.

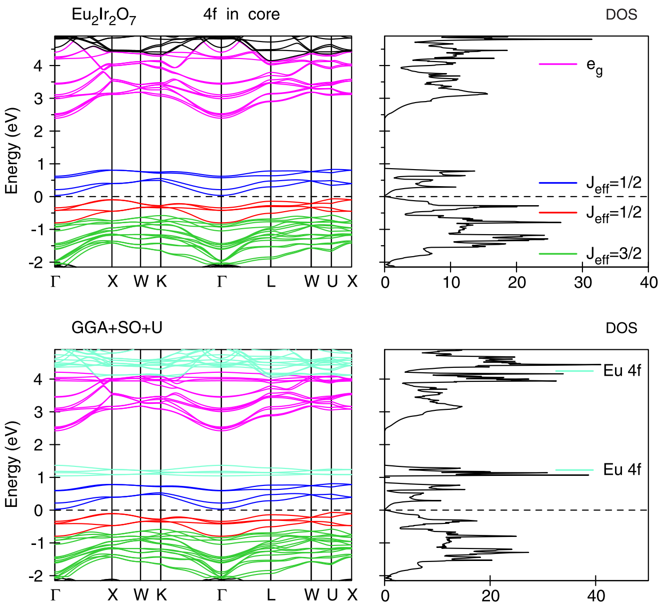

FIG. 6. The *ab initio* energy band structure and total DOS [in states/(cell eV)] of $Eu_2Ir_2O_7$ calculated in the GGA+SO approximation with fully localized $4f$ states in core (upper panel) and in the GGA+SO+U approach with partly localized $4f$ states (lower panel).

B. Magnetic structure

All the possible magnetic structures in the pyrochlore iridates $R_2Ir_2O_7$ (space group $Fd\bar{3}m$) can be classified by finding the magnetic co-representation for the tetrahedron group, which leads to $c\Gamma_{\rm mag} = c\Gamma_{3+} + c\Gamma_{5+} + c\Gamma_{7+} + c\Gamma_{9+}$ [69,70] (see Fig. 3 in Ref. [70]). Inspection reveals that $c\Gamma_{3+}$ corresponds to the AFM structure observed in FeF_3 [18], $c\Gamma_{5+}$ to the linear combination observed in the model XY pyrochlore antiferromagnet $Er_2Ti_2O_7$ [71], $c\Gamma_{7+}$ to the manifold of states proposed as the ground state for the Heisenberg pyrochlore antiferromagnet with dipole terms [70], and $c\Gamma_{9+}$ to the spin-ice-like manifold observed in the noncollinear ferromagnetic pyrochlores such as $Dy_2Ti_2O_7$ [72].

We found that the one-dimensional $c\Gamma_{3+}$ representation with the so-called "all-in/all-out" AFM configuration is the ground magnetic state in $Y_2Ir_2O_7$ (Fig. 7), which is in agreement with previous studies [11,33,34,73–75]. Disseler [75] shows that the experimentally observed results of zero-field muon spin relaxation in $Y_2Ir_2O_7$ are consistent only with a magnetically ordered Ir^{4+} sublattice with the AIAO magnetic structure and that the electronic state of Ir^{4+} is best described by the $J_{\rm eff} = 1/2$ model with local spin magnetic moments $M_s = 0.32\mu_B$/Ir, which is nearly identical to that expected for an Ir^{4+} ion with $J_{\rm eff} = 1/2$ in the $Y_2Ir_2O_7$ electronic configuration, where $\langle\mu\rangle = gJ\mu_B = 1/3\ \mu_B$. Our band structure calculations provide the spin magnetic moment equal to 0.316 μ_B at the Ir site in $Y_2Ir_2O_7$, which is in good agreement with the estimations from μSR measurements [75] and supports the nearly pure $J_{\rm eff} = 1/2$ character in $Y_2Ir_2O_7$.

We found that the one-dimensional $c\Gamma_{3+}$ representation with the AIAO AFM configuration is also the ground magnetic state in the $Pr_2Ir_2O_7$ compound in both the Ir and Pr

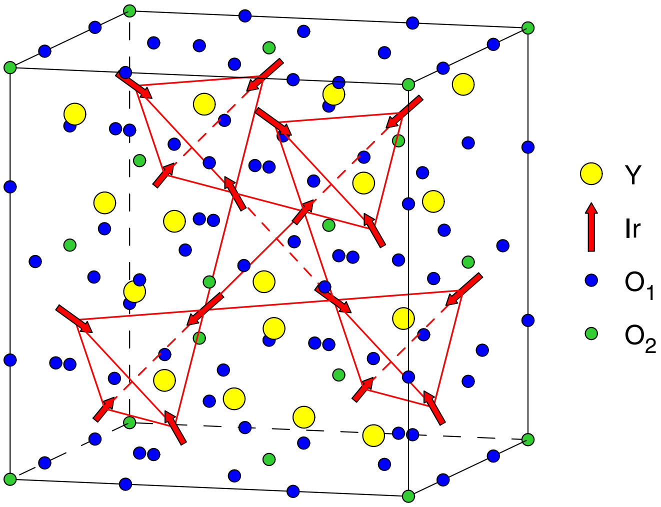

FIG. 7. The spin AIAO magnetic structure in $Y_2Ir_2O_7$.

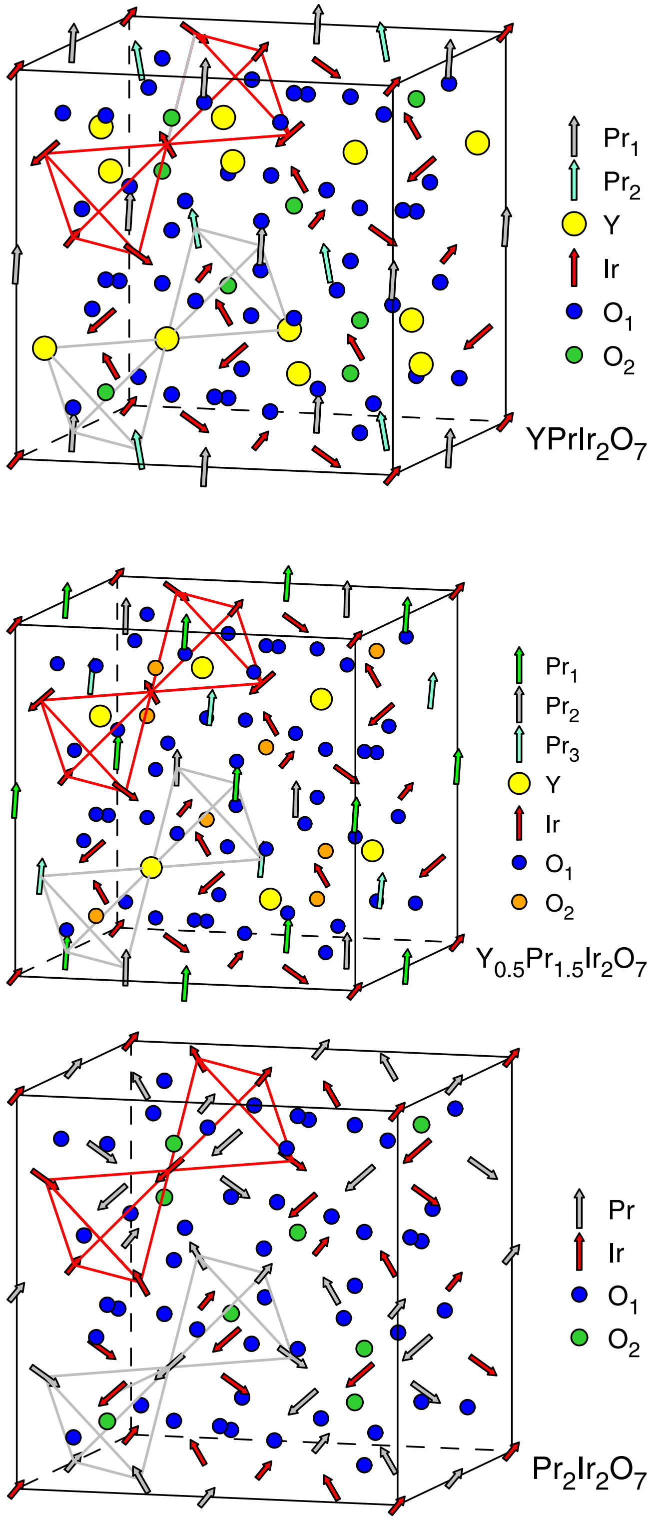

FIG. 8. The spin magnetic structures in the $(Y_{1-x}Pr_x)_2Ir_2O_7$ pyrochlore iridates for $x = 0$ (lower panel), $x = 0.75$ (middle panel), and $x = 0.5$ (upper panel).

sublattices (see the lower panel of Fig. 8). Due to the lack of Pr ions in the $(Y_{1-x}Pr_x)_2Ir_2O_7$ ($x = 0.75$ and 0.5) compounds their magnetic structures differ from the parent $Pr_2Ir_2O_7$ compound. The Pr^{3+} sublattice possesses the $c\Gamma_{9+}$ (Ψ_{11}) magnetic structure with a spin magnetic moments ordering along the z direction with a small deviation from the c axis for all three Pr ions in the $Y_{0.5}Pr_{1.5}Ir_2O_7$ pyrochlore (the middle panel of Fig. 8). The $PrYIr_2O_7$ compound possesses two nonequivalent Pr sites. We found two solutions with FM and AFM orderings of the Pr_1 and Pr_2 ions with a very small difference in their total energies, however, the FM ordering has a slightly lower energy. The Ir^{4+} sublattice possesses the $c\Gamma_{7+}$ (Ψ_5) AFM ordering in the $(Y_{1-x}Pr_x)_2Ir_2O_7$ ($x = 0.5$ and 0.75) compounds.

We found that the $Eu_2Ir_2O_7$ compound possesses several symmetry protected magnetic configurations such as $c\Gamma_{3+}$ and $c\Gamma_{7+}$ for both or one of the Ir or Eu sites. They have very close total energies which differ from each other just by several meV. However, the AIAO ($c\Gamma_{3+}$) configuration for both the Ir and Eu sites is the ground state in $Eu_2Ir_2O_7$, which is in agreement with previous studies [73,74,76].

IV. Ir L_3 RIXS SPECTRA

Figure 9 presents the experimentally measured RIXS spectra (open magenta circles) at the Ir L_3 edge for $R_2Ir_2O_7$ (R = Y, Pr, and Eu) compared with the theoretically calculated ones in the GGA+SO+U approximation (full blue lines) as well as the partial contributions from different interband transitions. The experimentally measured RIXS spectra of all the three compounds in Fig. 9 in addition to the elastic scattering peak at 0 eV possess sharp features below 2 eV, corresponding to transitions within the Ir t_{2g} levels, and a strong intense peak stretching from 2.5 to 5 eV that according to the calculations corresponds to d-d transitions between the Ir t_{2g} and e_g manifolds.

The double peak structure from 0.3 eV to 1.3 eV at the Ir L_3 edge in the $R_2Ir_2O_7$ (R = Y, Pr, and Eu) can be assigned to the local excitation between the filled $J_{\rm eff} = 1/2$ and empty $J_{\rm eff} = 1/2$ states. More precisely, the incoming photon excites a $2p_{3/2}$ core electron into a higher energy upper energy band state (empty $J_{\rm eff} = 1/2$) what is followed by a de-excitation from the lower energy band manifold (occupied $J_{\rm eff} = 1/2$) into the core level. The energy difference of the two low-lying peaks, $\Delta E = E_2 - E_1$, represents the splitting of the empty upper energy band manifold. Similar situation was found also for $In_2Ir_2O_7$ pyrochlore iridate. The excitations at low energy, labeled in Ref. [32] as E_1 and E_2, correspond to the transitions between the filled $J_{\rm eff} = 1/2$ and empty $J_{\rm eff} = 1/2$ states; the latter states are split into two subbands (not shown).

The GGA+SO approach without taking into account Coulomb correlations produces the metallic ground state in $Y_2Ir_2O_7$; as a result, the low energy double peak structure is situated at lower energy in comparison with the experimental measurements. A similar situation occurs also for $Pr_2Ir_2O_7$ and $Eu_2Ir_2O_7$ compounds where the GGA+SO approximation also places the low energy double peak structure at lower energy in comparison with the experiment (see the dashed black curves in Fig. 9). Panel (c) in Fig. 9 presents the theoretically calculated RIXS spectra for $YPrIr_2O_7$ and $Y_{0.5}Pr_{1.5}Ir_2O_7$. The low energy structure at around 0.9 eV transforms into a single intensive peak in these compounds due to a smaller splitting of the empty upper energy band (compare the blue lines in the lower and middle panels of Fig. 3). The experimental measurements of the RIXS

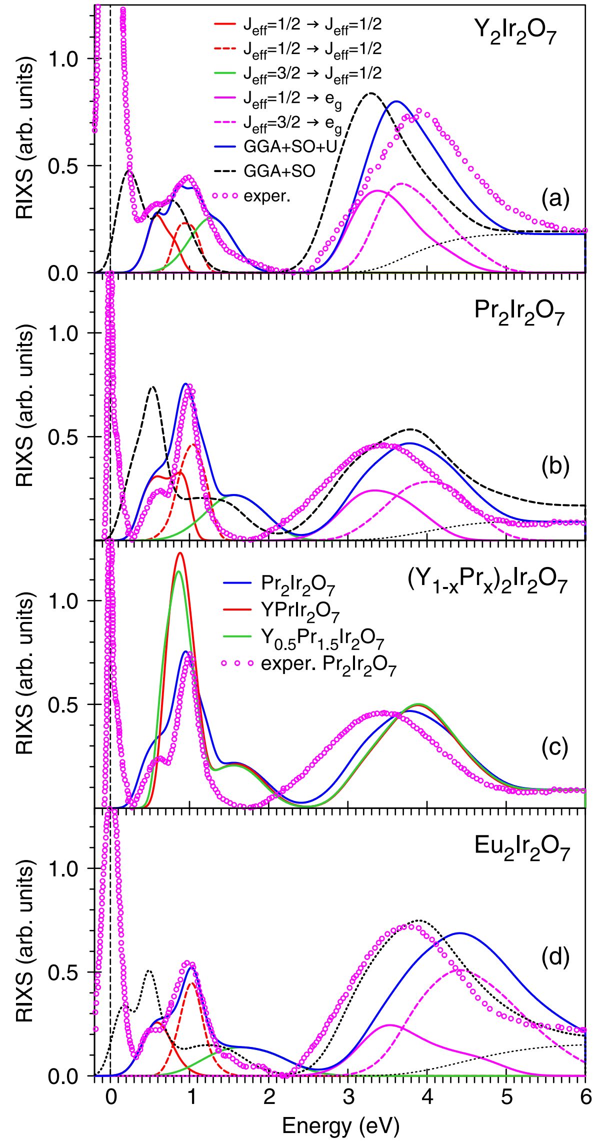

FIG. 9. The experimental RIXS spectra (open magenta circles) at the Ir L_3 edges for $Y_2Ir_2O_7$ [35] (a), $Pr_2Ir_2O_7$ [38] (b), and $Eu_2Ir_2O_7$ [38] (d) compared with the theoretical spectra (full blue lines) and the partial contributions from different interband transitions calculated in the GGA+SO+U approximation; the dashed black curve at the top panel presents the theoretical RIXS spectrum at the Ir L_3 edge for $Y_2Ir_2O_7$ calculated in the GGA+SO approximation. Panel (c) presents the theoretically calculated RIXS spectra for the $YPrIr_2O_7$ (red line) and $Y_{0.5}Pr_{1.5}Ir_2O_7$ (green line) compounds in comparison with the theoretical (blue line) and experimental (open magenta circles) RIXS spectra of $Pr_2Ir_2O_7$.

spectra at the Ir L_3 edge in solid solution pyrochlore iridates $(Y_{1-x}Pr_x)_2Ir_2O_7$ is highly desirable.

The fine structure situated in the 1.3–2.3 eV energy interval is due to the local excitation between the filled $J_{\mathrm{eff}} = 3/2$ and empty $J_{\mathrm{eff}} = 1/2$ states. Such a fine structure is observed in the experimental RIXS spectra from 1.5 eV to 2.1 eV in $Y_2Ir_2O_7$ and $Eu_2Ir_2O_7$ and it is very small in $Pr_2Ir_2O_7$. The intensity of this structure is overestimated in our band structure calculations. The strong intense peak stretching from 2.5 to 5 eV according to the calculations corresponds to $J_{\mathrm{eff}} = 1/2 \rightarrow e_g$ (full magenta lines) and $J_{\mathrm{eff}} = 3/2 \rightarrow e_g$ (dashed magenta lines) transitions. The GGA+SO+U calculations underestimate the energy position of the peak corresponding to the transitions between the Ir t_{2g} and e_g manifolds in $Y_2Ir_2O_7$ and overestimate it in $Pr_2Ir_2O_7$ and $Eu_2Ir_2O_7$. On the other hand, the energy position of this high energy structure is very sensitive to the sample preparation and sample quality. For example, the energy positions of this peak in Hozoi *et al.* [35] and Clancy *et al.* [38] measurements differ from each other by approximately 0.5 eV.

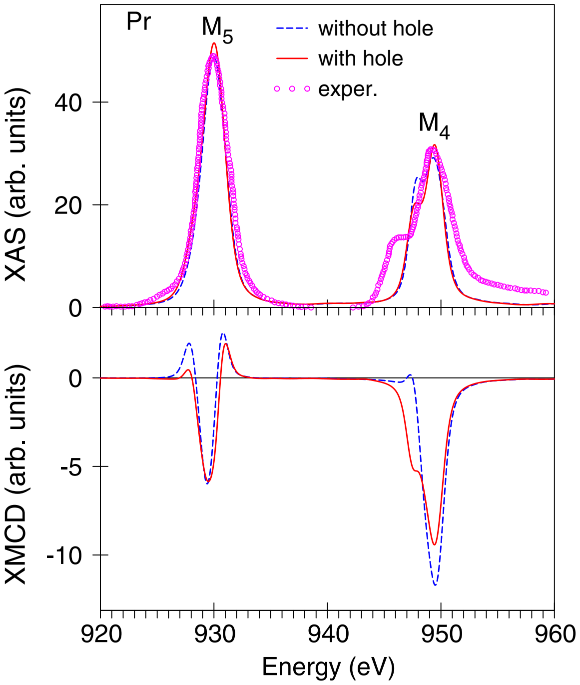

FIG. 10. Top panel: the experimental x-ray absorption spectra at the Pr $M_{4,5}$ edges for $Pr_2Ir_2O_7$ [24] (open circles) compared with the theoretically calculated spectra with (full red curves) and without core-hole effect; lower panel: the theoretically calculated Pr $M_{4,5}$ XMCD spectra with (full red curves) and without core-hole effect.

V. X-RAY ABSORPTION AND XMCD SPECTRA IN $Pr_2Ir_2O_7$

The study of the $4f$ electron shell in rare earth compounds is usually performed by tuning the energy of the x ray close to the $M_{4,5}$ edges of rare earth where electronic transitions between $3d_{3/2,5/2}$ and $4f_{5/2,7/2}$ states are involved. Figure 10 shows the experimentally measured by Kumar *et al.* [24] Pr $M_{4,5}$ XAS spectra along with theoretically calculated XAS (the upper panel) and XMCD spectra (the lower panel) (full blue curves) for $Pr_2Ir_2O_7$. The positions of the M_5 and M_4 XAS peaks are found to be around 930 and 949.3 eV, respectively, and they closely match those for Pr^{3+} ions, because the corresponding peak positions for Pr^{4+} occur at higher energy [24,77]. This suggests that Pr is in the 3+ charge state and thus shows agreement with the Ir^{4+} charge state. The theoretically calculated and experimental XAS spectra at the M_5 edge have a rather simple line shape composed of almost symmetrical white line peaks. The GGA+SO+U calculations

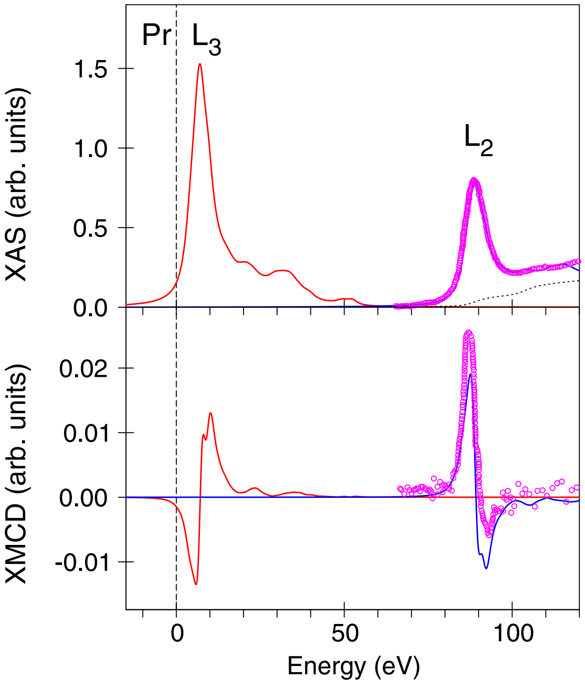

FIG. 11. The theoretically calculated x-ray absorption (upper panel) and XMCD spectra (lower panel) at the Pr $L_{2,3}$ edges compared with the experimental L_2 spectra measured on the $Pr_2Ir_2O_7$ thin film [39] (open circles). The theoretically calculated and experimental L_2 XAS and XMCD spectra are shifted by −400 eV to present both the L_2 and L_3 spectra in the same energy window. The dotted black curve in the upper panel shows the background scattering intensity.

show good agreement in the shape of the Pr XAS spectrum at the M_5 edge with the experimental measurements. They also reproduce the observed two peak structure of the Pr XAS spectrum at the M_4 edge, however, the theory underestimates the energy split between these two peaks. We found minor influence of the final-state interaction on the shape of the Pr $L_{2,3}$ XAS spectra in the whole energy interval. The dichroism at the Pr $M_{4,5}$ edges is very large (it amounts to more than 20% of the edge jump of the corresponding isotropic XAS spectra) due to the strong spin-orbit coupling of the initial Pr $3d$ core states and the large spin polarization of the final empty $4f_{5/2,7/2}$ states. We found that the XMCD spectra at the Pr M_5 and M_4 edges are of quite a different shape and intensity (see the lower panel in Fig. 10). The M_5 XMCD spectrum has a three peak structure and smaller intensity in comparison with one negative peak of relatively large intensity in the Pr M_4 spectrum. The core-hole effect modifies the XMCD low energy peaks at both the Pr M_5 and M_4 edges. The experimental measurements of the XMCD spectra at the Pr $M_{4,5}$ edges is highly desirable.

Figure 11 shows the theoretically calculated x-ray absorption (the upper panel) and XMCD spectra (the lower panel) at the Pr $L_{2,3}$ edges compared with the experimental L_2 spectrum measured under 5 T magnetic field on the $Pr_2Ir_2O_7$ thin film [39] (open circles). Both the Pr L_3 ($2p_{3/2} \rightarrow 5d_{5/2}$ transitions) and L_2 ($2p_{1/2} \rightarrow 5d_{3/2}$ transitions) XA spectra have a major peak at around 8 eV above the Fermi level and several high energy shoulders. The theory represents well all the fine structures of the observed experimental L_2 XA spectrum.

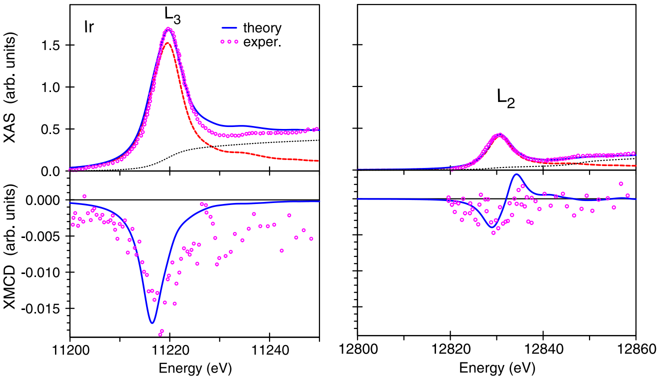

FIG. 12. The experimental x-ray absorption (upper panels) and XMCD spectra (lower panels) at the Ir $L_{2,3}$ edges in the $Pr_2Ir_2O_7$ thin film (magenta circles) [39] measured at 2 K under 5 T magnetic field compared with the theoretically calculated spectra in the GGA+SO+U approximation (full blue curves). The dotted black curves in the upper panels show the background scattering intensity.

The XMCD spectrum of Pr at the L_3 edge can be approximated by the following sum of m_j-projected partial densities of states [48]: $(N^{5/2}_{-5/2} + N^{5/2}_{-3/2}) - (N^{5/2}_{3/2} + N^{5/2}_{5/2})$. Here we use the notation $N^{j}_{m_j}$ for the density of states with the total momentum j and its projection m_j. From this expression one would expect an L_3 XMCD spectrum with two peaks of opposite signs with almost the same intensity. The corresponding L_2 XMCD spectrum can be approximated by the following partial DOS's: $(N^{3/2}_{-1/2} + N^{3/2}_{-3/2}) - (N^{3/2}_{1/2} + N^{3/2}_{3/2})$. From this expression one would also expect a two peak L_2 XMCD spectrum with a positive and a negative peak. Besides, due to the reversal energy sequences for the $j = 3/2$ and $j = 5/2$ sublevels the energy positions of the positive and negative peaks are opposite to each other for the L_3 and L_2 XMCD spectra. Our GGA+SO+U calculations overestimate the negative lobe and underestimate the positive one at the L_2 edge. There are no experimental measurements of the XAS and XMCD spectra at the Pr L_3 edge. We found minor influence of the final-state interaction on the shape of the Pr $L_{2,3}$ XMCD spectra in the whole energy interval. The small core-hole effect might come from the fact that the Pr $5d$ states are less localized in comparison with the $4f$ states and have smaller amplitude inside the MT sphere and thus are less subject to the core hole potential.

Figure 12 presents the experimental x-ray absorption (the upper panels) and XMCD spectra (the lower panels) measured at 2 K under 5 T magnetic field at the Ir $L_{2,3}$ edges in the $Pr_2Ir_2O_7$ [39] in comparison with the theoretically calculated spectra in the GGA+SO+U approximation (full blue curves). The theoretically calculated Ir $L_{2,3}$ XAS are in good agreement with the experiment. Our calculations show that the Ir $L_{2,3}$ XAS are dominated by the empty e_g states with a small contribution from the empty t_{2g} orbitals at lower energy. The XMCD, however, mainly comes from the t_{2g} orbitals ($J_{\mathrm{eff}} = 1/2$). This results in a shift between the XAS and XMCD maxima of the order of the cubic crystal field splitting Δ_{CF}. The GGA+SO+U approach describes well the shape and

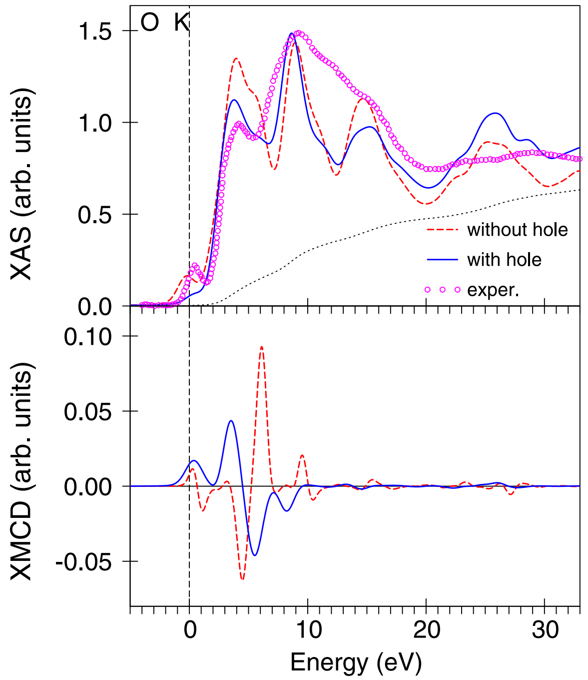

FIG. 13. Top panel: the experimental x-ray absorption spectrum at the O *K* edge for $Pr_2Ir_2O_7$ [24] (open circles) compared with the theoretically calculated spectra in the GGA+SO+U approximation with (full blue curve) and without (dashed red curve) taking into account the core-hole effect. The dotted black curve shows the background scattering intensity; lower panel: the theoretically calculated O *K* XMCD spectra with (full blue curve) and without (dashed red curve) taking into account the core-hole effect.

intensity of the circular dichroism at the Ir $L_{2,3}$ edges. The XMCD signal at the L_2 edge, which is much smaller relative to L_3, suggests that the Ir 5*d* electronic state in the $Pr_2Ir_2O_7$ thin film is close to the $J_{\rm eff} = 1/2$ state.

Figure 13 shows the experimental x-ray absorption spectrum (the upper panel) at the O *K* edge for $Pr_2Ir_2O_7$ [24] (open circles) compared with the theoretically calculated spectra in the GGA+SO+U approximation with (the full blue curve) and without (the red dashed curve) taking into account the core-hole effect. The O *K* XA spectrum extends over more then 30 eV and has the fine structures typical for the oxygen *K* absorption in various transition metal oxides [65]. The inclusion of the core-hole effect in the calculations slightly improves the agreement with the experimental spectrum, especially the peak at around 3–4 eV.

The exchange splitting of the initial 1*s*-core state is extremely small [78], therefore only the exchange and spin-orbit splitting of the final 2*p* states is responsible for the observed dichroism at the oxygen *K* edge. For this reason the dichroism is found to be very small. The spin magnetic moments at the O_1 and O_2 sites are aligned opposite to each other and equal to 0.0630 μ_B and -0.0122 μ_B, respectively. The orbital magnetic moments were found to be equal to 0.099 μ_B and -0.0003 μ_B for the O_1 and O_2 sites, respectively. The O *K* XMCD spectrum (the lower panel of Fig. 13) possesses a quite complicated structure with several minima and maxima. Due to larger spin and orbital moments the O_1 sites produce an almost one order of magnitude larger XMCD signal than the O_2 sites. The dichroism at the O *K* edge is significant only for 2*p* states, which strongly hybridize with Ir 5*d* states in the 3.5–7.0 eV energy interval above the Fermi level (see Fig. 4). The spectral XMCD features between 7 and 35 eV, which are due to the O 2*p* orbitals hybridized with Ir *s* and *p* orbitals, are extremely small.

The core-hole effect alters the O *K* XMCD spectrum to larger extent than the XA spectrum. We investigated also the effect of the electric quadrupole E_2 and magnetic dipole M_1 transitions on the XAS and XMCD spectra at the oxygen *K* edge. We found that the M_1 transitions are extremely small in comparison with the E_2 transitions and can be neglected. The E_2 transitions indeed contribute to the high energy XAS and XMCD spectra, although the quadrupole E_2 transitions are more than two orders of magnitude smaller than the electric dipole transitions E_1. The experimental measurements of the XMCD spectrum at the O *K* edge is highly desirable.

VI. CONCLUSIONS

The electronic and magnetic structures, RIXS spectra and x-ray magnetic circular dichroism of the pyrochlore iridates $Y_2Ir_2O_7$, $Pr_2Ir_2O_7$, and $Eu_2Ir_2O_7$ were investigated theoretically within a DFT-GGA approach in the frame of the fully relativistic spin-polarized Dirac LMTO band-structure method with taking into account Coulomb electron-electron correlations.

The GGA+SO approximation produces a metallic ground state in $Y_2Ir_2O_7$, in contradiction with resistivity measurements which claim that $Y_2Ir_2O_7$ is a spin-orbit Mott insulator. To produce the insulating ground state we use the GGA+U method. The Coulomb repulsion U splits the half-filled $J_{\rm eff} = 1/2$ band producing an empty upper energy band with pure $d_{5/2}$ character well separated from a lower $J_{\rm eff} = 1/2$ energy band and $J_{\rm eff} = 3/2$ states below the Fermi level. We found that the insulator $Y_2Ir_2O_7$ possesses nearly pure $J_{\rm eff} = 1/2$ character with only a small admixture of the $J_{\rm eff} = 3/2$ component in the $J_{\rm eff} = 1/2$ bands.

The IrO_6 octahedron is trigonally compressed in the pyrochlore iridates $R_2Ir_2O_7$, which decreases the Ir-O-Ir angle in the neighboring IrO_6 octahedra. Larger A-site ions tend to result in a smaller distortion, which is responsible for increased hopping and an increased band width which leads to a stronger metallic character. With increasing the size of A cations from Y^{3+} to Pr^{3+} the system becomes a semimetal and remains metallic down to the lowest temperature. Besides, the admixture of the $J_{\rm eff} = 3/2$ component to the $J_{\rm eff} = 1/2$ states is increased with going from $Y_2Ir_2O_7$ to $Pr_2Ir_2O_7$.

We found that the structure of the Ir t_{2g} energy bands is almost identical in $Y_2Ir_2O_7$, $Pr_2Ir_2O_7$, and $Eu_2Ir_2O_7$, which can explain why these compounds exhibit qualitatively similar RIXS spectra. Another very important feature is the split of the empty upper energy bands ($J_{\rm eff} = 1/2$) in all three compounds under consideration. The split is the smallest in $Y_2Ir_2O_7$ and the largest in $Eu_2Ir_2O_7$. Such a splitting is responsible for the fine structure of the low energy peak in the corresponding RIXS spectra.

We investigated the evolution of the electronic structure in the solid solution pyrochlore iridates $(Y_{1-x}Pr_x)_2Ir_2O_7$

($x = 0.25$, 0.5, and 0.75). With Y substitution the magnetic-insulating state in $Y_2Ir_2O_7$ ($x = 0.0$) is weakened, and $(Y_{1-x}Pr_x)_2Ir_2O_7$ possesses a metal-insulator transition for $x = 0.75$ in agreement with the Kumar *et al.* [24] measurements who observed a metal-insulator transition for the $x = 0.8$ sample.

We found that the one-dimensional $c\Gamma_{3+}$ representation with the AIAO AFM configuration is the ground magnetic state in $Y_2Ir_2O_7$ as well as in $Pr_2Ir_2O_7$. Due to the lack of Pr ions in the $Y_{0.5}Pr_{1.5}Ir_2O_7$ and $YPrIr_2O_7$ compounds their magnetic structures differ from the parent $Pr_2Ir_2O_7$ compound. The Pr^{3+} sublattice possesses the $c\Gamma_{9+}$ (Ψ_{11}) magnetic structure in $YPrIr_2O_7$. The $Y_{0.5}Pr_{1.5}Ir_2O_7$ compound possesses two nonequivalent Pr sites. We found two solutions with FM and AFM orderings of the Pr_1 and Pr_2 ions along the z direction with a very small difference in their total energies, however, the FM ordering has a slightly lower energy. The Ir^{4+} sublattice possesses the $c\Gamma_{7+}$ (Ψ_5) AFM ordering in the $(Y_{1-x}Pr_x)_2Ir_2O_7$ ($x = 0.5$ and 0.75) compounds.

We found that the $Eu_2Ir_2O_7$ compound possesses several symmetry protected magnetic configurations such as $c\Gamma_{3+}$ and $c\Gamma_{7+}$ for both or one of the Ir or Eu sites. They have very close total energies which differ from each other just by several meV. However, the AIAO ($c\Gamma_{3+}$) configuration for both the Ir and Eu sites is the ground state in $Eu_2Ir_2O_7$.

The experimentally measured RIXS spectra of all three compounds in addition to the elastic scattering peak at 0 eV possess sharp features below 2 eV corresponding to transitions within the Ir t_{2g} levels, and a strong intense peak stretching from 2.5 to 5 eV that according to the calculations corresponds to d-d transitions between the Ir t_{2g} and e_g manifolds. The double peak structure from 0.3 eV to 1.3 eV can be assigned to the local excitations between the filled $J_{\text{eff}} = 1/2$ and empty $J_{\text{eff}} = 1/2$ states which are split into two subbands. The fine structure situated in the 1.3–2.3 eV energy interval is due to the local excitation between the filled $J_{\text{eff}} = 3/2$ and empty $J_{\text{eff}} = 1/2$ states. The intensity of this structure is overestimated in our band structure calculations.

We found that the GGA+SO+U approach with $U_{\text{eff}} = 1.5$ eV at the Ir site and $U_{\text{eff}} = 6.3$ eV for the Pr site describes well the XAS and XMCD spectra at the Ir $L_{2,3}$, Pr $L_{2,3}$, and O K edges. Our calculations show that the Ir $L_{2,3}$ XA spectra are dominated by the empty e_g states with a small contribution from the empty t_{2g} orbitals at lower energy. The XMCD, however, mainly comes from the t_{2g} orbitals ($J_{\text{eff}} = 1/2$). This results in a shift between the XAS and XMCD maxima of the order of the cubic crystal field splitting Δ_{CF}. The XMCD signal at the L_2 edge which is much smaller relative to L_3 suggests that the Ir $5d$ electronic state in the $Pr_2Ir_2O_7$ thin film is close to the $J_{\text{eff}} = 1/2$ state.

We found minor influence of the final-state interaction on the shape of the Pr $L_{2,3}$ and $M_{4,5}$ XAS and Pr $L_{2,3}$ XMCD spectra. The core-hole effect modifies the XMCD low energy peaks at both the Pr M_5 and M_4 edges.

The dichroism at the oxygen K edge is very small because only the exchange and spin-orbit splitting of the final $2p$ states is responsible for it. The largest contribution to the XMCD signal at the O K edge comes from the first neighbors of the Ir ions, namely, the O_1 ions which possess the largest spin and orbital moments. The dichroism is significant only for $2p$ states, which strongly hybridize with Ir $5d$ states in the 3.5–7.0 eV energy interval above the Fermi level. The spectral XMCD features between 7 and 35 eV, which are due to the O $2p$ orbitals hybridized with Ir s and p orbitals, are extremely small. We found that the electric quadrupole E_2 transitions are more than two orders of magnitude smaller than the electric dipole transitions E_1, and the magnetic dipole M_1 transitions are much smaller in comparison with the E_2 transitions.

ACKNOWLEDGMENTS

D.A.K. gratefully acknowledges the hospitality at the Max-Planck-Institut für Festkörperforschung in Stuttgart during his stay there. The studies were supported by the National Academy of Sciences of Ukraine within the budget program KPKBK 6541230-3A “Support for the development of priority areas of scientific research.”

---

[1] M. J. P. Gingras, C. V. Stager, N. P. Raju, B. D. Gaulin, and J. E. Greedan, Phys. Rev. Lett. **78**, 947 (1997).
[2] S. Yoshii and M. Sato, J. Phys. Soc. Jpn. **68**, 3034 (1999).
[3] S. Nakatsuji, Y. Machida, Y. Maeno, T. Tayama, T. Sakakibara, J. van Duijn, L. Balicas, J. N. Millican, R. T. Macaluso, and J. Y. Chan, Phys. Rev. Lett. **96**, 087204 (2006).
[4] H. Fukazawa, R. G. Melko, R. Higashinaka, Y. Maeno, and M. J. P. Gingras, Phys. Rev. B **65**, 054410 (2002).
[5] X.-P. Yao and G. Chen, Phys. Rev. X **8**, 041039 (2018).
[6] D. Pesin and L. Balents, Nat. Phys. **6**, 376 (2010).
[7] B.-J. Yang and Y. B. Kim, Phys. Rev. B **82**, 085111 (2010).
[8] W. Witczak-Krempa, T. P. Choy, and Y. B. Kim, Phys. Rev. B **82**, 165122 (2010).
[9] A. Go, W. Witczak-Krempa, G. S. Jeon, K. Park, and Y. B. Kim, Phys. Rev. Lett. **109**, 066401 (2012).
[10] G. Chen and M. Hermele, Phys. Rev. B **86**, 235129 (2012).
[11] X. Wan, A. M. Turner, A. Vishwanath, and S. Y. Savrasov, Phys. Rev. B **83**, 205101 (2011).
[12] W. Witczak-Krempa and Y. B. Kim, Phys. Rev. B **85**, 045124 (2012).
[13] L. Balents, Physics **4**, 36 (2011).
[14] W. Witczak-Krempa, G. Chen, Y. B. Kim, and L. Balents, Annu. Rev. Condens. Matter Phys. **5**, 57 (2014).
[15] O. Vafek and A. Vishwanath, Annu. Rev. Condens. Matter Phys. **5**, 83 (2014).
[16] Y. Machida, S. Nakatsuji, Y. Maeno, T. Tayama, T. Sakakibara, and S. Onoda, Phys. Rev. Lett. **98**, 057203 (2007).
[17] S. B. Lee, A. Paramekanti, and Y. B. Kim, Phys. Rev. Lett. **111**, 196601 (2013).
[18] E.-G. Moon, C. Xu, Y. B. Kim, and L. Balents, Phys. Rev. Lett. **111**, 206401 (2013).
[19] S. M. Disseler, C. Dhital, A. Amato, S. R. Giblin, C. de la Cruz, S. D. Wilson, and M. J. Graf, Phys. Rev. B **86**, 014428 (2012).

[20] M. C. Shapiro, S. C. Riggs, M. B. Stone, C. R. de la Cruz, S. Chi, A. A. Podlesnyak, and I. R. Fisher, Phys. Rev. B **85**, 214434 (2012).

[21] W. K. Zhu, M. Wang, B. Seradjeh, F. Yang, and S. X. Zhang, Phys. Rev. B **90**, 054419 (2014).

[22] H. Kumar and A. K. Pramanik, J. Magn. Magn. Mater. **478**, 148 (2019).

[23] V. K. Dwivedi and S. Mukhopadhyay, J. Appl. Phys. **126**, 165112 (2019).

[24] H. Kumar, K. C. Kharkwal, K. Kumar, K. Asokan, A. Banerjee, and A. K. Pramanik, Phys. Rev. B **101**, 064405 (2020).

[25] Y. Tokiwa, J. J. Ishikawa, S. Nakatsuji, and P. Gegenwart, Nat. Mater. **13**, 356 (2014).

[26] Y. Machida, S. Nakatsuji, S. Onoda, T. Tayama, and T. Sakakibara, Nature (London) **463**, 210 (2010).

[27] T. Ohtsuki, Z. Tian, M. Halim, S. Nakatsuji, and M. Lippmaa, J. Appl. Phys. **127**, 035303 (2020).

[28] T. Kondo, M. Nakayama, R. Chen, J. J. Ishikawa, E.-G. Moon, T. Yamamoto, Y. Ota, W. Malaeb, H. Kanai, Y. Nakashima *et al.*, Nat. Commun. **6**, 10042 (2015).

[29] H. Kumar, R. Chaurasia, P. Kumari, and A. K. Pramanik, AIP Conf. Proc. **1942**, 130058 (2018).

[30] F. F. Tafti, J. J. Ishikawa, A. McCollam, S. Nakatsuji, and S. R. Julian, Phys. Rev. B **85**, 205104 (2012).

[31] Z. Tian, Y. Kohama, T. Tomita, H. Ishizuka, T. H. Hsieh, J. J. Ishikawa, K. Kindo, L. Balents, and S. Nakatsuji, Nat. Phys. **12**, 134 (2016).

[32] A. Krajewska, T. Takayama, R. Dinnebier, A. Yaresko, K. Ishii, M. Isobe, and H. Takagi, Phys. Rev. B **101**, 121101(R) (2020).

[33] H. Shinaoka, S. Hoshino, M. Troyer, and P. Werner, Phys. Rev. Lett. **115**, 156401 (2015).

[34] H. Zhang, K. Haule, and D. Vanderbilt, Phys. Rev. Lett. **118**, 026404 (2017).

[35] L. Hozoi, H. Gretarsson, J. P. Clancy, B.-G. Jeon, B. Lee, K. H. Kim, V. Yushankhai, P. Fulde, D. Casa, T. Gog *et al.*, Phys. Rev. B **89**, 115111 (2014).

[36] D. Uematsu, H. Sagayama, T. H. Arima, J. J. Ishikawa, S. Nakatsuji, H. Takagi, M. Yoshida, J. Mizuki, and K. Ishii, Phys. Rev. B **92**, 094405 (2015).

[37] C. Donnerer, M. C. Rahn, M. M. Sala, J. G. Vale, D. Pincini, J. Strempfer, M. Krisch, D. Prabhakaran, A. T. Boothroyd, and D. F. McMorrow, Phys. Rev. Lett. **117**, 037201 (2016).

[38] J. P. Clancy, H. Gretarsson, E. K. H. Lee, D. Tian, J. Kim, M. H. Upton, D. Casa, T. Gog, Z. Islam, B.-G. Jeon *et al.*, Phys. Rev. B **94**, 024408 (2016).

[39] L. Guo, N. Campbell, Y. Choi, J.-W. Kim, P. J. Ryan, H. Huyan, L. Li, T. Nan, J.-H. Kang, C. Sundahl *et al.*, Phys. Rev. B **101**, 104405 (2020).

[40] L. J. P. Ament, M. van Veenendaal, T. P. Devereaux, J. P. Hill, and J. van den Brink, Rev. Mod. Phys. **83**, 705 (2011).

[41] V. V. Nemoshkalenko, A. E. Krasovskii, V. N. Antonov, V. N. Antonov, U. Fleck, H. Wonn, and P. Ziesche, Phys. Status Solidi B **120**, 283 (1983).

[42] E. Arola, P. Strange, and B. L. Gyorffy, Phys. Rev. B **55**, 472 (1997).

[43] E. Arola, M. Horne, P. Strange, H. Winter, Z. Szotek, and W. M. Temmerman, Phys. Rev. B **70**, 235127 (2004).

[44] G. Lehmann and M. Taut, Phys. Status Solidi B **54**, 469 (1972).

[45] P. E. Blöchl, O. Jepsen, and O. K. Andersen, Phys. Rev. B **49**, 16223 (1994).

[46] D. A. Kukusta and A. N. Yaresko, in *Resonant Inelastic X-Ray Scattering Spectra from Band Structure Calculations*, Workshop "Strongly Correlated Electron Systems," Ringberg Castle, Germany, 2018 (unpublished).

[47] V. N. Antonov, O. Jepsen, A. N. Yaresko, and A. P. Shpak, J. Appl. Phys. **100**, 043711 (2006).

[48] V. N. Antonov, B. N. Harmon, A. N. Yaresko, and A. P. Shpak, Phys. Rev. B **75**, 184422 (2007).

[49] V. N. Antonov, A. N. Yaresko, and O. Jepsen, Phys. Rev. B **81**, 075209 (2010).

[50] B. J. Ruck, H. J. Trodahl, J. H. Richter, J. C. Cezar, F.Wilhelm, A. Rogalev, V. N. Antonov, B. D. Le, and C. Meyer, Phys. Rev. B **83**, 174404 (2011).

[51] O. K. Andersen, Phys. Rev. B **12**, 3060 (1975).

[52] A. Y. Perlov, A. N. Yaresko, and V. N. Antonov, PY-LMTO, A Spin-polarized Relativistic Linear Muffin-tin Orbitals Package for Electronic Structure Calculations, 1995 (unpublished).

[53] J. P. Perdew, K. Burke, and M. Ernzerhof, Phys. Rev. Lett. **77**, 3865 (1996).

[54] A. N. Yaresko, V. N. Antonov, and P. Fulde, Phys. Rev. B **67**, 155103 (2003).

[55] V. I. Anisimov and O. Gunnarsson, Phys. Rev. B **43**, 7570 (1991).

[56] I. V. Solovyev, P. H. Dederichs, and V. I. Anisimov, Phys. Rev. B **50**, 16861 (1994).

[57] P. H. Dederichs, S. Blügel, R. Zeller, and H. Akai, Phys. Rev. Lett. **53**, 2512 (1984).

[58] W. E. Pickett, S. C. Erwin, and E. C. Ethridge, Phys. Rev. B **58**, 1201 (1998).

[59] M. Cococcioni and S. de Gironcoli, Phys. Rev. B **71**, 035105 (2005).

[60] K. Nakamura, R. Arita, Y. Yoshimoto, and S. Tsuneyuki, Phys. Rev. B **74**, 235113 (2006).

[61] F. Aryasetiawan, M. Imada, A. Georges, G. Kotliar, S. Biermann, and A. I. Lichtenstein, Phys. Rev. B **70**, 195104 (2004).

[62] I. V. Solovyev and M. Imada, Phys. Rev. B **71**, 045103 (2005).

[63] V. P. Antropov, V. N. Antonov, L. V. Bekenov, A. Kutepov, and G. Kotliar, Phys. Rev. B **90**, 054404 (2014).

[64] F. Aryasetiawan, K. Karlsson, O. Jepsen, and U. Schonberger, Phys. Rev. B **74**, 125106 (2006).

[65] V. Antonov, B. Harmon, and A. Yaresko, *Electronic Structure and Magneto-Optical Properties of Solids* (Kluwer, Dordrecht, 2004).

[66] V. N. Antonov, S. Uba, and L. Uba, Phys. Rev. B **98**, 245113 (2018).

[67] V. N. Antonov, D. A. Kukusta, S. V. Moklyak, D. V. Mazur, and L. V. Bekenov, Phys. Rev. B **101**, 054441 (2020).

[68] J. L. Campbell and T. Parr, At. Data Nucl. Data Tables **77**, 1 (2001).

[69] O. V. Kovalev, H. T. Stokes, and D. M. Hatch, *Representations of the Crystallographic Space Groups*, 2nd ed. (Yverdon, Switzerland; Philadelphia, Pa., USA: Gordon and Breach, 1993).

[70] A. S. Wills, M. E. Zhitomirsky, B. Canals, J. P. Sanchez, P. Bonville, P. Dalmas de Réotier, and A. Yaouanc, J. Phys.: Condens. Matter **18**, L37 (2006).

[71] J. D. M. Champion, A. S. Wills, T. Fennell, S. T. Bramwell, J. S. Gardner, and M. A. Green, Phys. Rev. B **64**, 140407(R) (2001).

[72] M. J. Harris, S. T. Bramwell, D. F. McMorrow, T. Zeiske, and K. W. Godfrey, Phys. Rev. Lett. **79**, 2554 (1997).

[73] H. Sagayama, D. Uematsu, T. Arima, K. Sugimoto, J. J. Ishikawa, E. O'Farrell, and S. Nakatsuji, Phys. Rev. B **87**, 100403(R) (2013).

[74] H. Takatsu, K. Watanabe, K. Goto, and H. Kadowaki, Phys. Rev. B **90**, 235110 (2014).

[75] S. M. Disseler, Phys. Rev. B **89**, 140413(R) (2014).

[76] Y. Wang, H. Weng, L. Fu, and X. Dai, Phys. Rev. Lett. **119**, 187203 (2017).

[77] Z. Hu, G. Kaindl, H. Ogasawara, A. Kotani, and I. Felner, Chem. Phys. Lett. **325**, 241 (2000).

[78] H. Ebert, J. Phys.: Condens. Matter **1**, 9111 (1989).